

AD-AU48 753

NAVAL RESEARCH LAB WASHINGTON D C
INTENSE FOCUSED ION BEAMS AND THEIR INTERACTION WITH MATTER.(U)
NOV 77 D MOSHER, G COOPERSTEIN

F/G 20/7

UNCLASSIFIED

NRL-MR-3658

SBIE-AD-E000 082

NL

| 0f |

ADAO48 753



AD A 048753

decoo002

12 NW

NRL Memorandum Report 3658

Intense Focussed Ion Beams and Their Interaction with Matter

D. MOSHER, G. COOPERSTEIN, S. J. STEPHANAKIS,
SHYKE A. GOLDSTEIN, D. G. COLOMBANT and ROSWELL LEE

Plasma Physics Division

November 1977

This research was sponsored by the Defense Nuclear Agency under
subtask T99QAXLA014, work unit 46, and work unit title Ion Beam Generation.



NAVAL RESEARCH LABORATORY
Washington, D.C.

Approved for public release; distribution unlimited.

DDC
RECEIVED
JAN 19 1978
B

AD No. _____
DDC FILE COPY

SECURITY CLASSIFICATION OF THIS PAGE (When Data Entered)

REPORT DOCUMENTATION PAGE		READ INSTRUCTIONS BEFORE COMPLETING FORM
1. REPORT NUMBER NRL Memorandum Report 3658	2. GOVT ACCESSION NO.	3. RECIPIENT'S CATALOG NUMBER
4. TITLE (and Subtitle) INTENSE FOCUSED ION BEAMS AND THEIR INTERACTION WITH MATTER.	5. TYPE OF REPORT & PERIOD COVERED Interim report on a continuing NRL problem	
7. AUTHOR(s) D. Mosher, G. Cooperstein, S. J. Stephanakis, Shyke A. Goldstein, D. G. Colombant and Roswell Lee	6. PERFORMING ORG. REPORT NUMBER	
9. PERFORMING ORGANIZATION NAME AND ADDRESS Naval Research Laboratory Washington, D. C. 20375	8. CONTRACT OR GRANT NUMBER(s)	
11. CONTROLLING OFFICE NAME AND ADDRESS Defense Nuclear Agency Washington, D. C. 20305	10. PROGRAM ELEMENT, PROJECT, TASK AREA & WORK UNIT NUMBERS NRL Problem H02-26A DNA Subtask T99QAXLA014	
14. MONITORING AGENCY NAME & ADDRESS (if different from Controlling Office) 12 27p.	12. REPORT DATE November 1977	
	13. NUMBER OF PAGES 29	
	15. SECURITY CLASS. (of this report) UNCLASSIFIED	
	15a. DECLASSIFICATION/DOWNGRADING SCHEDULE	
16. DISTRIBUTION STATEMENT (of this Report) Approved for public release; distribution unlimited. 14 NRL-MR-3658		
17. DISTRIBUTION STATEMENT (of the abstract entered in Block 20, if different from Report) 16 T99QAXL 17 A014 19 AD-E000 082 B 18 SBIE		
18. SUPPLEMENTARY NOTES This research was sponsored by the Defense Nuclear Agency under subtask T99QAXLA014, work unit 46, and work unit title Ion Beam Generation. This report contains the text of a paper presented at the 2nd International Topical Conference on (Continues)		
19. KEY WORDS (Continue on reverse side if necessary and identify by block number) Ion beam focussing Beam propagation Target hydrodynamics Thin foil anodes		
20. ABSTRACT (Continue on reverse side if necessary and identify by block number) Recent experiments and theory dealing with the production, focussing, and interaction with matter of ion beams extracted from pinched-beam diodes is reviewed. Present experiments indicate that in excess of 300 kA of .8 MeV protons can be extracted from flat anode structures while deuterons can be focussed to about 70 kA/cm ² over 2 cm ² target areas in a focussing geometry. sg.cm.		

DDC
RECEIVED
JAN 19 1978
RECEIVED

DD FORM 1 JAN 73 1473

EDITION OF 1 NOV 65 IS OBSOLETE
S/N 0102-014-6601

SECURITY CLASSIFICATION OF THIS PAGE (When Data Entered)

251 950

AB

18. Supplementary Notes (Continued)

High Power Electron and Ion Beam Research and Technology, held at Cornell University, Ithaca, N. Y. on October 3-5, 1977.

†Science Applications, Inc., McLean, Virginia 22101

CONTENTS

I. INTRODUCTION	1
II. REVIEW OF RECENT RESEARCH	2
III. TARGET HYDRODYNAMICS	6
IV. NEW RESULTS	10
V. DISCUSSION	13
VI. REFERENCES	16

ACCESSION for		
NTIS	White Section	<input checked="" type="checkbox"/>
DDC	Buff Section	<input type="checkbox"/>
UNANNOUNCED		<input type="checkbox"/>
JUSTIFICATION		
BY		
DISTRIBUTION/AVAILABILITY CODES		
Dist.	A BIL 200/01	SPECIAL
A		

INTENSE FOCUSED ION BEAMS AND THEIR INTERACTION WITH MATTER

I. Introduction

Recent work¹ has demonstrated that large relativistic-electron-beam accelerators can be used to create proton beams with efficiencies comparable to that of electron beams and that such ion beams are well suited to drive thermonuclear pellets². Since ions have a much shorter range in materials than electrons of comparable energy, higher impedance, i.e. technologically simpler, generators can be employed to create ion beams of fusion-level (100 TW) power. The favorable deposition characteristic of ions (maximum energy deposition occurs deep within the target) allows for the design of efficient pellets with low beam-power and large focussing-area requirements. Additionally, unlike either laser or electron-beam drivers, 100% of the ion-beam energy is delivered to the target in a known fashion, independent of any plasma-dynamic or electromagnetic effects which are difficult to determine theoretically. Thus, the ability of a particular pulsed-power system to couple the required energy into a pellet can be assessed before construction of the facility.

Before light ions can be seriously considered for fusion-reactor applications, a number of important technical capabilities must be demonstrated. These are the abilities to: (1) scale beam power to the 100 TW level, (2) focus the beam to pellet dimensions, and (3) propagate the

Note: Manuscript submitted November 14, 1977.

beam over many meters to demonstrate standoff between accelerator and pellet. The primary purpose of this paper is to review recent work and present new experimental and theoretical research which indicate that the first two achievements can be accomplished. Techniques for attaining the third ability³ are the subject of the next paper. Section II reviews recent experiments on ion production and ballistic focussing with supporting analytical and numerical-simulation results. Section III discusses two models for the interaction of focussed ion beams with sub-range-thick foil targets and compares theory with experimental results using the beams discussed in Section II. Experimental findings of the last few months are presented in Section IV, while the results of research are discussed in Section V.

II. Review of Recent Research

Several years ago, in an effort to theoretically model intense electron-beam pinching in low-impedance diodes, Goldstein and Lee⁴ determined that radial electron flow enhanced ion emission from the anode plasma by an amount far in excess of the Child-Langmuir rate. They derived the relation

$$\frac{I_i}{I_e} > \frac{R}{2d} \left(\frac{2eV}{m_i c^2} \right)^{\frac{1}{2}} \quad (1)$$

for the ratio of ion to electron current flowing in a self-pinched diode. In Eq. (1), R is the cathode radius, d is the diode gap, and V is the diode voltage. Later, particle-simulation codes⁵ confirmed this relation. For the parameters of the Naval Research Laboratory Gamble II

operated at $\frac{1}{2}$ TW (800 kV, 600 kA), Eq. (1) predicts that roughly $\frac{1}{2}$ of the total diode current ($I_i + I_e \approx 600$ kA) should be carried by protons. Experiments¹ conducted on Gamble II operating in reverse polarity (cathode at ground potential) yielded results consistent with Eq. (1). Nuclear activation of carbon targets was used to measure up to 200 kA of 0.8 MeV protons in the configuration shown in Fig. 1A.

Figure 2 shows the scaling of ion-beam power with 1 Ω -generator power obtained by solving Eq. (1) simultaneously with a generator circuit equation and a modified para-potential-flow equation⁶ for diode current.

$$I = I_i + I_e = 5.5 \times 10^3 (R/d) \gamma \ln [\gamma + (\gamma^2 - 1)^{\frac{1}{2}}] \quad (2)$$

$$V_o = V + I Z_G \quad (3)$$

Here, γ is the electron relativistic factor, V_o is the generator open-circuit voltage, and Z_G is the characteristic generator impedance. The abscissa is the product IV while the ordinate is $I_i V$. The NRL and lower-power Sandia Laboratory experimental results are in reasonable agreement with the theoretical scaling. At the 100 TW level, about 60% of the available energy is predicted to be converted to ion energy. Results presented in Section IV employing newer designs indicate that 50% efficiency can be achieved currently at Gamble II power levels. Thus, there is good reason to believe that ion-beam powers at the 100 TW level are attainable.

Because of their high mass, simple ballistic focussing of ions can be used to concentrate the beam down to pellet dimensions. Preliminary

NRL results using small diameter hemispherical anodes and transmission cathodes⁷ demonstrated the experimental validity of the technique. In more recent experiments, focussing was accomplished by curving the anode (1.6 mm-thick Lucite) and transmission cathode into sections of spheres of larger radii. The geometry employed for this is shown in Fig. 1C. Experiments were performed both with and without a curved 2 μ m Kimfoil polycarbonate foil mounted inside the aluminum ring cathode. Both configurations focussed the ion beam to pellet dimensions⁸.

Beam cross-section as a function of axial position was determined qualitatively by placing thin, plastic target foils perpendicular to the beam at various axial positions and taking 100 ns framing photographs of the visible light emitted (Fig. 3). These show decreasing beam size up to the best-focus location (upper-right photograph) where beam diameters in the 1-2 cm range were recorded. Framing photographs through a side-viewing port (center photograph) of the luminosity produced by passing the focussed beam through ~ 3 Torr of air are consistent with the focussed-ion trajectories determined by the foil measurements. A more accurate determination of beam size was obtained by placing thick aluminum targets at the best-focus location. The resulting rear surface spall, an example of which is shown in Fig. 4, indicates focussed-beam diameters of about 1 cm. Implications of ion-induced spall with respect to ion-current density are mentioned in Section III.

Proton-current-density as a function of radius at the best focus was determined by activation of carbon located behind thick targets with varying-diameter holes located at the focus. Results comparing radial

distributions using flat and focussing anodes are shown in Fig. 5. Both the central current density and fraction of the total current contained within a 2 cm-diameter hole increased by about a factor of six as the anode was changed from flat to curved. Typically, 20-30 kA/cm² proton current density was recorded for the central .75 cm² of the focussed beam. Prompt-neutron measurements obtained by focussing a deuteron beam onto a 1.3 cm² CD target resulted in 15-20 kA/cm². The results reflect the atomic-mass scaling of Eq. (1) in that deuteron fluxes are down by about the square-root of the ion mass from the proton fluxes.

Bare aluminum x-ray diodes⁹ were employed to determine the intensity of radiation emitted by sub-range metal-foil targets placed at the best-focus location. Absolute calibration of the diodes was obtained by assuming the targets emitted black-body spectra. An example of these measurements is shown in Fig. 6. Here, it is shown that the x-ray intensity remains constant as the viewing area is reduced down to 1.3 cm² again demonstrating ion-focussing down to at most this cross-sectional area. The intensity of the radiation was that of a 9 eV black-body radiator for sub-range gold targets. As will be shown in the next section, the x-ray measurements predict focussed-current densities of 30-40 kA/cm², in fair agreement with activation results.

All of the focus measurements described above indicate that best focussing occurred several centimeters closer to the anode than the location of the geometric focus. Two possible causes for this were errors in curvature and magnetic deflection of ions in the diode region.

The effect of magnetic deflection was tested using the NRL 2-d, time-dependent diode code¹⁰. Results of this calculation are shown in Fig. 7. There, the self-consistently calculated ion trajectories have been ballistically projected axially assuming a spherically-curved anode surface. The effect of the diode electromagnetic fields is seen to smear the focus both axially and radially. As observed in experiments, about $\frac{1}{3}$ of the calculated focussed current appears within a 1 cm^2 area. However, the shift in focus observed in experiments is a factor of 2-3 greater than predicted in the code. It will be shown in Section IV that improvements in anode curvature and the use of thin-foil transmission cathodes in Series II anode structures (Fig. 1D) bring experiment closer to theoretical prediction.

III. Target Hydrodynamics

Here, it is desired to calculate the hydrodynamic response of sub-range foil targets and use the resulting dependence of radiation-intensity on ion-current density as a diagnostic for the focussing experiments. Two plasma models are discussed and compared. The first is a zero-dimensional, similarity solution to the equations of motion while the second is a one-dimensional solution in a slab geometry using a MHD fluid code. Both approaches assume that the plasma is in Saha equilibrium¹¹ and radiates like a black body; a reasonable assumption for the low-temperature, high-atomic-number plasmas of interest. Ion stopping-power and range information is provided by analytic fits to published

tables¹². The time variation of ion energy and current density are taken from Gamble II electrical measurements¹. The similarity solutions are discussed first.

The conservation of target-mass and momentum equations

$$\frac{\partial \rho}{\partial t} + \frac{\partial}{\partial z} (\rho V) = 0 \quad (4)$$

$$\rho \left(\frac{\partial V}{\partial t} + V \frac{\partial V}{\partial z} \right) = - \frac{\partial P}{\partial z} \quad (5)$$

where ρ , V , and P are the plasma mass density, fluid velocity and pressure are solved by writing P in the form $P = a(\rho, T)\rho$ and requiring that $a(\rho, T)$ varies slowly with z compared to ρ . This is insured by seeking a solution for which T , the plasma temperature, is constant for all z but varies in time. The variation of $a(\rho, T)$ with z is then due only to the slow change in ionization level with density associated with Saha equilibrium. Solutions to Eqs. (4) and (5) may then be written

$$\rho(z, t) = \frac{\Delta}{\pi^{\frac{1}{2}} Z(t)} \exp(-z^2/Z^2) \quad (6)$$

$$V(z, t) = \dot{Z}z/Z \quad (7)$$

where the evolution of Z in time is given by

$$Z\ddot{Z} = 2a(\rho, T) \quad (8)$$

Here, $\bar{\rho}$ is an average density, and Δ is the foil-plasma thickness in g/cm². The initial value of Z is determined from the requirement that $\rho(0, 0)$ be the solid mass-density ρ_s , i.e. $Z(0) = \Delta \left(\frac{1}{\pi^{\frac{1}{2}} \rho_s} \right)^{-1}$.

The evolution of plasma temperature with time is calculated from overall energy balance. The sum of the total plasma kinetic and internal energies must equal the difference between absorbed beam energy and black-body radiated energy. If $b(\bar{\rho}, T)$ is the average internal energy per gram determined from Saha equilibrium, this relation takes the form

$$\int_{-\infty}^{+\infty} \rho \left[\frac{1}{2} V^2 + b \right] dz = \int_0^t (\bar{\Phi} \Delta \mathcal{E}_1 - 2\sigma T^4) dt' \quad (9)$$

In Eq. (9), $\bar{\Phi}$ is the incident ion flux and $\Delta \mathcal{E}_1$ is the total energy loss suffered by an ion traversing the plasma. Integrating over z results in

$$\frac{1}{2} \dot{Z}^2 + b(\bar{\rho}, T) = \frac{2}{\Delta} \int_0^t (\bar{\Phi} \Delta \mathcal{E}_1 - 2\sigma T^4) dt' \quad (10)$$

which is solved simultaneously with Eq. (8) to obtain the temporal variations of Z and T .

The results of the similarity solutions are to be compared with those of a 1-D Eulerian code solving conservation of mass, momentum, and energy equations on an inhomogeneous grid. The major advantage of this more complicated approach is the realistic treatment of local energy conservation resulting in self-consistent temperature distribution. The energy balance equation includes diffusive transport of black-body radiation, electron heat conduction, and a time-varying ion deposition profile. Radiation is transported to within one optical depth (based on the Rosseland mean-free-path¹³) of free space at which point it is freely-radiated at the local temperature.

Figure 8 compares the variation of peak density and temperature with time for the two models discussed when the target is a 5.8 mg/cm^2 gold foil with 30 kA/cm^2 maximum proton current incident. This thickness is about .6 of the range of an .8 MeV proton and was commonly used in the experiment. The solid curves in the figure show the variation of ρ and T using the similarity solutions while the points show results of the MHD code. The triangles plot the change in maximum temperature in the interior of the plasma, while the rectangles show the variation in radiation temperature (located one optical depth inside the plasma). The asymmetry in heating associated with the ion deposition profile is recorded by the height of the rectangles. The upper edge records the radiation temperature at the back of the plasma (where ion heating is maximized) while the lower edge shows that of the blow-off plasma facing the incident beam. The convergence of the two radiation temperatures late in time is due to the low-energy of incident protons. At that time, protons are stopped in the plasma interior so that reduced heating of the back-plasma surface occurs. Figure 8 also illustrates why rear-surface spall (Fig. 4) requires high ion-current densities ($> 10 \text{ kA/cm}^2$). Peak pressure always occurs very early in the beam pulse because of rapid plasma expansion.

The general agreement between the two models is gratifying considering their difference in sophistication. The single-temperature similarity solution falls between the maximum and radiation temperatures predicted by the 1D code. The variation in peak temperature occurring

in the pulse with peak incident ion-current density is shown in Fig. 9. The temperature from the OD, the maximum from the 1D, and an average radiation temperature $\bar{T}^4 = \frac{1}{2}(T_1^4 + T_2^4)$ are plotted. Based on this result and absolute measurements of soft x-ray intensity (see Fig. 6), it was determined that 30-40 kA/cm² maximum proton-current density was incident on the foil and that the gold foils radiate at about 9eV. Similar calculations yielded about 50 kA/cm² for x-radiation from aluminum foils. However, measurements conducted with transmission-window-filtered x-ray diodes indicated that the increase in radiation intensity might be associated with aluminum L-line radiation. The current density inferred from gold-foil measurements agrees with other proton measurements conducted on Series I diodes and discussed in Section II.

IV. New Results

Here, proton- and deuteron-beam measurements using the Series II flat and focussing geometries shown in Figs. 1B and 1D are discussed. Modifications common to both new designs are: (1) a thin-foil reflexing structure extending beyond the cathode radius, (2) a controlled gap (typically 5 mm) between the foil anode and anode back-plate, and (3) the use of an aluminum or carbon button (typically 1.3 cm in diameter) providing on-axis electrical continuity between foil and anode back-plate. Proton yield was found to increase as the foil-backplate gap was increased from zero when foils which allowed electrons to reflex were employed. However, gaps much in excess of 5 mm led to poor quality, as asymmetric electron pinches with associated decrease in ion yield. With the optimal gap, the central button effectively symmetrized the electron

pinch on axis but its removal did not reduce ion yields. The support ring across which the anode foil was stretched was made of either aluminum or Lucite. Ion yield did not depend on the ring's material nor its removal (when the foil was supported by the central button).

In the flat geometry of Fig. 1B, carbon activation was used to determine proton yields for CH_2 anode foils ranging from 2.5×10^{-3} to .05 cm thick. Anode-cathode gaps were 4-5 mm. No statistically-significant variation of proton current with foil thickness was observed. The maximum ion current, inferred from activation, electrical measurements and Eqs. (1) and (2) averaged .32 MA for these data with a standard deviation of about .1 MA. The corresponding values of total proton yield were in the range $(1.3 \pm .4) \times 10^{17}$ with ion-pulse durations of 60-90 ns. These data demonstrate that nearly one half of the diode current can be routinely extracted as protons.

The observed high ion-production efficiency is supported by new numerical-simulation results studying ion enhancement due to electron reflexing in thin-foil anodes. Reflexing is modeled by including the energy loss of electrons passing through CH_2 foils and by assuming that electron motion behind the foil is determined by the local magnetic field with zero electric field. The diode geometry shown in Fig. 10 with $V_D = 750$ kV was simulated for various anode-foil thicknesses. The table shows that the ratio I_i/I_e increases and that the total diode current decreases as the foil thickness is reduced.

Series II focussing anodes (Fig. 1D) were modified in two additional ways. They were fabricated from .025 to .050 cm thick polyvinyl acetate

and were configured to a much more accurate spherical section than the Lucite Series I structures. The accurate spherical contour was desired to eliminate errors in curvature as a source of degradation of ion focussing. In addition to electron reflexing, an additional advantage of the thinner structures is a greatly reduced pressure pulse following discharge allowing for proximity soft x-ray and other delicate diagnoses.

Ion focussing was tested using CD_2 -coated anodes and targets because of the difficulties in obtaining accurate carbon-activation data at high incident current densities¹. Totally-collecting CD_2 targets mounted just behind the hollow cathode in focussing geometry gave deuteron yields as high as 1.1×10^{17} corresponding to 200 kA average ion currents. Measurements with similar targets mounted 9.5 cm away from the anode indicated an about 30% reduction in deuteron number.

Best focus was determined by measuring the neutron yield from 1.9 cm^2 CD_2 targets mounted at various axial positions. Figure 11 shows neutron yield vs. distance from the anode using both hollow cathodes and cathodes containing 2μ -thick KIMFOL polycarbonate-transmission foils. The variation of yield with position is much closer to what one would expect (Fig. 7) than was obtained with Series I focussing anodes. That is, best focussing occurs at, and within a few centimeters in front of, the geometric focus. The improved agreement with theory is attributed to the highly-spherical contours employed in the latest experiments. The neutron yield at the 12 cm location for KIMFOL cathodes corresponds to an average deuteron current-density in excess of 70 kA/cm^2 over the 1.9 cm^2 target with as many as 5.5×10^{16} deuterons intercepted by it.

Thus, about $2/3$ of the deuterons reaching the axial location of the target were focussed inside 2 cm^2 . This figure is a factor-of-two improvement in focussing efficiency over either Series I focussing anodes (see Fig. 5) or Series II anodes with hollow cathodes.

Figure 12 helps one to understand the improved focussing attainable with KIMFOL cathodes. A current shunt was placed in the return-current chamber through which the beam passed and in which the target was mounted. On shots in which the cathode was hollow, net currents measured were close to total ion current. When KIMFOL was employed with focussing geometries, net currents were typically reduced by a factor-of-2.5 accompanied by a factor-of-2 increase in neutron yield. Although the nature of the electron flow is not presently understood, it is probable that the higher current non-neutralization associated with the bare cathode flow produces fields which disrupt the ballistic focussing of ions. This effect is not a serious impediment since a high degree of beam neutralization can be assured by a few Torr gas background in the focussing region.

V. Discussion

In the introduction, it was stated that the viability of light ions for inertial fusion depended on demonstrations of ion-production scaling, focusability, and transport. Here, significant progress in the first two of these areas has been demonstrated.

Measurements of proton currents from Series II flat anodes have demonstrated that about $1/2$ of the total diode current can be extracted

as ions. This represents a nearly factor-of-two improvement in efficiency over that predicted by the Goldstein-Lee formula Eq. (1) or the scaling of Fig. 2. PIC results suggest that this improvement can be traced to the use of thin-foil anode structures which allow for electron reflexing in the anode plane. In any case, the efficiency predicted for 100 TW-level generators has already been achieved on Gamble II at .5 TW.

Focussing measurements utilizing Series II focussing anodes coated with CD_2 have demonstrated a three-fold improvement in focussed-deuteron current density over that attainable with earlier designs. About $1/2$ of the total deuteron number produced in the diode was observed to be focussed with a 1.9 cm^2 area 12 cm from the anode, consistent with that predicted by numerical simulation. Additional improvements in focussing may require aspheric anode configurations in order to compensate for magnetic deflection in the diode. An upper limit of 4° beam divergence due to thermal, time varying-field, or scattering effects can be associated with the deuteron focussing results. As will be discussed in the next paper, this figure is sufficient to allow focussing over several-meter distances.

The most recent measurements have determined the importance of current neutralization to good focussing. The observed large net currents are not understood at this time although techniques for their reduction to safe levels are available. Employing KIMFOL transmission anodes reduces the net current to about 40% of the ion current, causing a

dramatic improvement in deuteron focussing. Future experiments will test the effect of reduction of net currents to much lower levels by providing a few Torr gas background in the focussing region.

VI. References

1. S. J. Stephanakis, D. Mosher, G. Cooperstein, J. R. Boller, J. Golden and S. A. Goldstein, Phys. Rev. Lett. 37, 1543 (1976).
2. M. J. Clauser, Phys. Rev. Lett. 34, 570 (1975).
3. D. Mosher in IEEE Conf. Record Abstracts of the 1977 International Conf. on Plasma Sci., May 23-25, 1977, Troy, N.Y.
4. S. A. Goldstein and R. Lee, Phys. Rev. Lett. 35, 1079 (1975).
5. J. W. Poukey, in Proceedings of the International Topical Conference on Electron Beam Research and Technology, Albuquerque, New Mexico, 1975.
6. G. Cooperstein and J. J. Condon, J. Appl. Phys. 46, 1535 (1975).
7. G. Cooperstein, S. J. Stephanakis, J. R. Boller, R. Lee and S. A. Goldstein, in Proceedings of the 1976 IEEE International Conference on Plasma Science, Austin, Texas, 1976.
8. S. J. Stephanakis, G. Cooperstein, S. A. Goldstein, D. Mosher and W. F. Oliphant, in IEEE Conf. Record Abstracts of the 1977 International Conf. on Plasma Sci., May 23-25, 1977, Troy, N. Y.
9. J. R. Kerns and D. J. Johnson, J. Appl. Phys. 45, 5225 (1974).
10. R. Lee and S. A. Goldstein, in IEEE Conf. Record Abstracts of the 1977 International Conf. on Plasma Sci., May 23-25, 1977, Troy, N.Y.
11. M. M. Widner, informal communication.
12. L. C. Northcliffe and R. F. Schilling, "Range and Stopping Power Tables for Heavy Ions," Texas A&M University Cyclotron Institute Report undated and unnumbered.

13. Y. B. Zeldovich and Y. P. Raizer, Physics of Shock Waves and High Temperature Phenomena, Academic Press, Vol. II (1966).

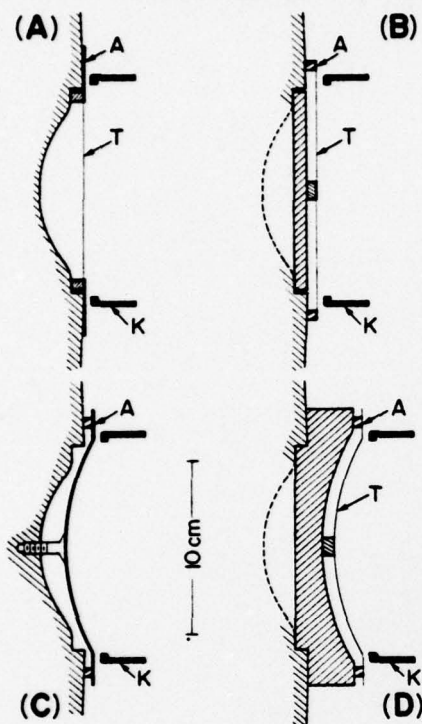
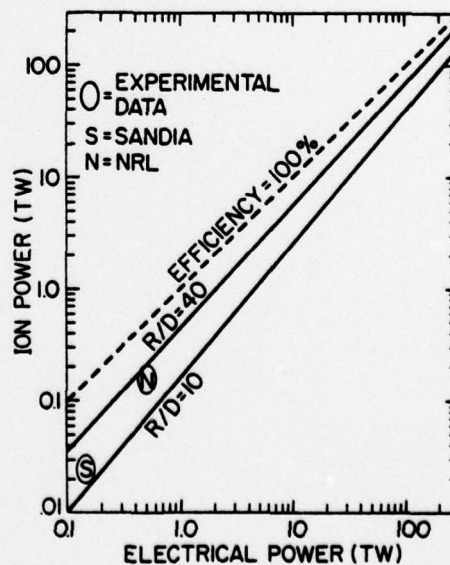


Fig. 1 - Diode configurations used in the experiment. (A) Series I-flat, (B) series II-flat, (C) series I-focussing, and (D) series II-focussing. Cathodes (K), anodes (A), and thin-foils (T) are labeled.

Fig. 2 - Theoretical scaling of ion power vs. deliverable electrical power for a 1Ω generator



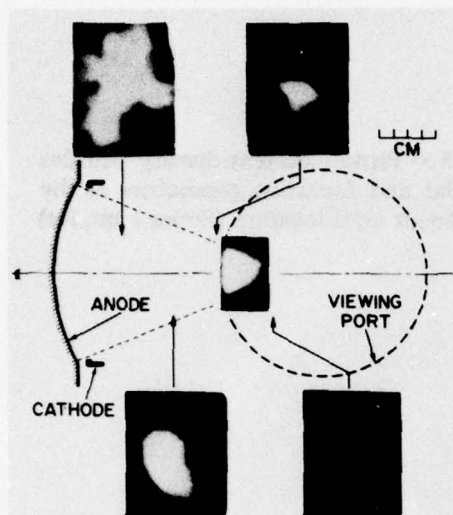


Fig. 3 — Visible-light framing photographs of ion-heated targets

Fig. 4 — Ion-induced rear-surface spall of an aluminum target placed at the ion focus



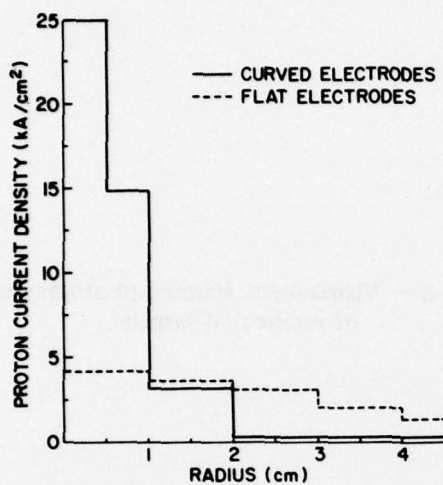
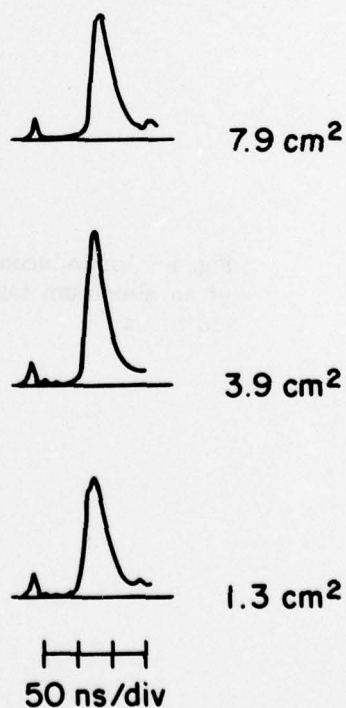


Fig. 5 — Proton current-density profiles for flat and focussing geometries at the best-focus axial location (Series I anodes)

Fig. 6 — X-ray diode traces of XUV emission from sub-ion-range gold targets mounted at the Series I focus for three target viewing areas



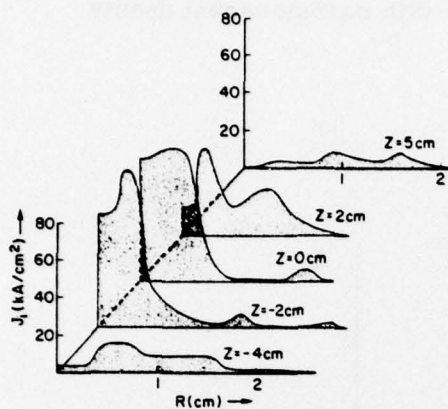
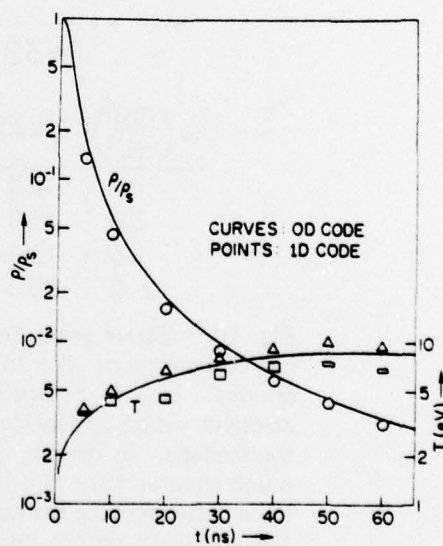


Fig. 7 — PIC-code prediction of the time-averaged ion-current-density distribution in radius for various axial locations. Diode parameters were $R/D = 20$, $V = .75$ MV.

Fig. 8 — Plasma density and temperature variations with time predicted by 0D and 1D fluid models. Response shown corresponds to 30 kA/cm^2 of $.8 \text{ MeV}$ protons incident on a 5.8 mg/cm^2 gold foil.



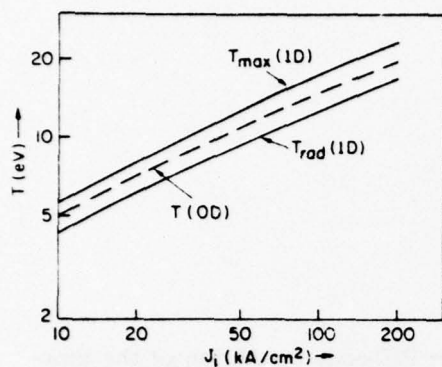
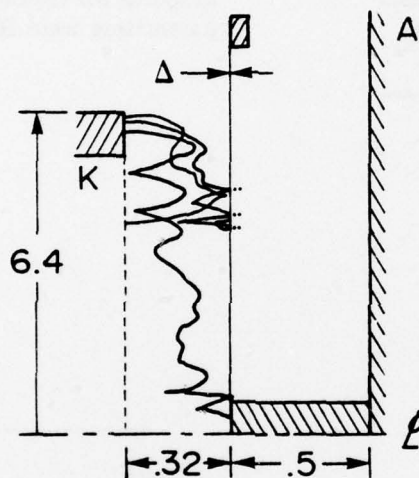


Fig. 9 — Variation of gold-plasma temperature with incident current density



$\Delta \left(\frac{\text{mg}}{\text{cm}^2} \right)$	$I_i(\text{kA})$	$I_e(\text{kA})$	$I_T(\text{kA})$
∞	125	435	560
38	150	385	545
13	190	310	500
2.5	265	210	475

Fig. 10 — Diode geometry and results of simulation of ion enhancement due to electron reflexing in thin-foil anodes. Due to compression of the radial dimension, electron orbits appear to intersect the anode normal to the surface. In reality, the radial momentum is usually much greater than the axial momentum and the electrons, after passing through the anode, execute a partial Larmor orbit before reappearing in the anode-cathode gap.

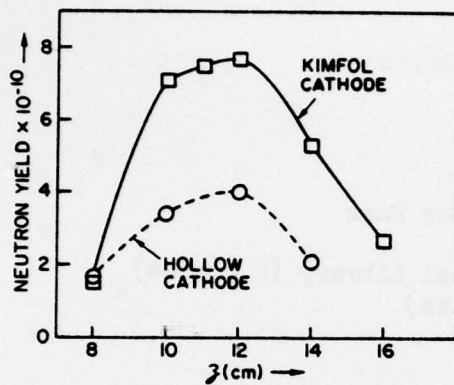
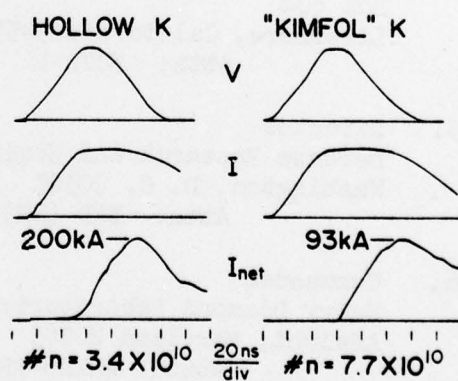


Fig. 11 — Variation of prompt-neutron yield from a 1.9 cm^2 target vs. axial distance from a Series II-focussing anode

Fig. 12 — Diode voltage, diode current, and net current variations with time for two of the shots of Fig. 11



DISTRIBUTION LIST

1. Director
Defense Advanced Research Projects Agency
Architect Building
1400 Wilson Boulevard
Arlington, Virginia 22209
Attn: LTC R. P. Sullivan
2. Director
Defense Nuclear Agency
Washington, D. C. 20305
Attn: DDST, Mr. Peter Haas
RATN
STTL, Technical Library (2 copies)
RAEV (2 copies)
STVL
STSI
3. Commander
Field Command
Defense Nuclear Agency
Albuquerque
Kirtland AFB, New Mexico 87115
Attn: FCPR
4. Chief
Field Command
Defense Nuclear Agency
Livermore Division
Box 808
Livermore, California 94550
Attn: FCPR-L
5. Director
Defense Research and Engineering
Washington, D. C. 20301
Attn: DAD (SK) Mr. G. R. Barse
6. Commander
Harry Diamond Laboratories
Adelphi, Maryland 20783
Attn: AMXDO-RBF, Mr. John Rosado
AMXDO-RBH, Mr. S. Graybill
AMXDO-RC, Dr. Robert Oswald, Chief, LAB 300

7. Air Force Weapons Laboratory, AFSC
Kirtland AFB, New Mexico 87117
Attn: DY, Dr. Guenther
EL, Mr. John Darrah
DYS, Dr. Baker
SAA
SUL, Technical Library
ELP, TREE Section
8. Space and Missile Systems Organization
Post Office Box 92960
Worldway Postal Center
Los Angeles, California 90009
Attn: SKT, Mr. Peter H. Stadler
RSP, System Defense and Assessment, LTC Gilbert
9. Sandia Laboratories
P. O. Box 5800
Albuquerque, New Mexico 87115
Attn: Document Control for 5220, Dr. J. V. Walker
Document Control for 5242, Dr. G. Yonas
Document Control for Technical Library
10. Aerospace Corporation
P. O. Box 92957
Los Angeles, California 90009
Attn: Mr. J. Benveniste
Dr. Gerald G. Comisar, Jr.
11. University of Texas
Fusion Research Center
Physics Building 330
Austin, Texas 78712
Attn: Dr. William E. Drummond
12. Battelle Memorial Institute
Columbus Laboratories
505 King Avenue
Columbus, Ohio 43201
Attn: Mr. P. Malozzi
13. Maxwell Laboratories, Inc.
9244 Balboa Avenue
San Diego, California 92123
Attn: Dr. P. Korn
14. Mission Research Corporation
735 State Street
Santa Barbara, California 93101
Attn: Dr. Conrad L. Longmire

15. Physics International Corporation
2700 Merced Street
San Leandro, California 94577
Attn: Document Control for Dr. Sidney Putnam
Document Control for Mr. Ian Smith
16. R & D Associates
P. O. Box 9695
Marina del Rey, California 90291
Attn: Dr. Bruce Hartenbaum
17. Science Applications, Inc.
P. O. Box 2351
La Jolla, California 92037
Attn: Dr. J. Robert Beyster
18. Stanford Research Institute
333 Ravenswood Avenue
Menlo Park, California 94025
Attn: Dr. Robert A. Armistead, Jr.
19. Dr. Victor A. J. Van Lint
Mission Research Corporation
7650 Convoy Court
San Diego, California 92111
20. Commander
Naval Surface Weapons Center
White Oak Laboratory
Silver Spring, Maryland 20910
21. DASIAC, GE Tempo
El Paseo Building
816 State Street
Santa Barbara, California 93102
22. DDC (2 copies)
23. Code 2628 (20 copies)
24. Code 7700
25. Code 7770 (20 copies)
26. Jaycor
205 South Whiting
Suite 500
Alexandria, Virginia 22304